

Supporting Information

Gold Nanocrystals and Conjugated-Polymer-Wrapped Single-Walled Carbon Nanotube Composites for Catalyzing CO₂ Electroreduction

Yueying Li,^{1,2} Ngoc Kim Dang,² Guorui Gao,² Homin Shin,¹ Shriya Sharma,² Xiaohua Wu,¹ Oltion Kodra,³ Andre Zborowski,³ Patrick R. L. Malenfant,¹ Jianfu Ding,¹, Cao-Thang Dinh,^{2,*} Jianying Ouyang^{1,*}

1. Quantum and Nanotechnologies Research Center, National Research Council Canada, 1200 Montreal Road, Ottawa, Ontario, K1A 0R6, Canada
2. Department of Chemical Engineering, Queen's University, Dupuis Hall, Kingston, Ontario, K7L 3N6, Canada
3. Clean Energy Innovation Research Centre, National Research Council Canada, 1200 Montreal Road, Ottawa, Ontario, K1A 0R6, Canada

Corresponding authors: Jianying.Ouyang@nrc-cnrc.gc.ca; caothang.dinh@queensu.ca

Table of contents

Table S1. Summary of eCO ₂ RR performance catalyzed by Au nanocrystals and nanoclusters	S4
Figure S1. Absorption spectra of PFBPpy/sc-SWCNT in THF before mixing, right after mixing, and overnight after mixing with AuCl ₃ THF solution.	S5
Figure S2. Size distribution histograms of AuNCs synthesized with varied [Au]/[BPpy]	S5
Figure S3. (a) TEM image of 1.65Au-PFDD/SWCNT sample, (b) High-resolution TEM image of 6.4Au-PFBPpy/SWCNT sample.	S6
Figure S4. XRD spectra of substrate background and 0.8Au-PFBPpy/SWCNT sample (left), and original spectra for the samples of 1.65Au-, 3.2Au-, and 6.4Au-PFBPpy/SWCNT (right)	S6
Figure S5. The comparison of ¹ H-NMR spectra in the backbone region of PFDD, PFBPpy, polymer/CNT control, and AuNCs-polymer/CNT complex (Au:BPpy = 3.7:1) in THF-d ₈	S7
Figure S6. The comparison of ¹ H-NMR spectra in the sidechain region of PFDD, PFBPpy, polymer/CNT control, and AuNCs-polymer/CNT complex (Au:BPpy = 3.7:1) in THF-d ₈	S8
Figure S7. ¹ H-NMR of PFDD (top) and PFBPpy (bottom) in THF-d ₈	S9
Figure S8. ¹ H-NMR of polymer/CNT control (top) and AuNCs-polymer/CNT complex (Au:BPpy = 3.7:1) (bottom) in THF-d ₈	S10
Figure S9. The comparison of FT-IR spectra of PFDD, PFBPpy, polymer/CNT control, and 1.65Au-PFBPpy/CNT composite	S11
Figure S10. SEM images of Sample 1.65Au-PFBPpy/SWCNTs dried at room temperature on silicon wafer (a), thermal treated at 270 °C for 3 hours on silicon wafer (b) and on carbon paper (c and d). Spectrum 106 and spectrum 107 are presented in (e) and (f)	S12
Figure S11. TGA curves of (a) PFDD, (b)PFBPpy with SWCNTs, (c) 1.65Au-PFBPpy/SWCNT, (d) Sigracet 39 BB carbon paper	S13
Figure S12. Linear sweep voltammetry (LSV) curves for the 1.65Au-PFBPpy/SWCNTs sample under various conditions, polymer/CNTs control sample, and 1.65Au-PFDD/SWCNTs sample	S14
Table S2. Impedance measured for samples with different drying temperature or compositions	S15
Figure S13. The CO/H ₂ ratio changes as a function of total current for various catalyst loading	S15

Figure S14. SEM images of Sample 1.65Au-PFBPy/SWCNTs after thermal treated at 270 °C for 3 hours on carbon paper before (**a1**) and after (**b1**) electrolysis (~3 hours). One local area showing numerous small particles with scattering big particles before (**a2**) and after (**b2**) electrolysis. The corresponding x-ray mapping for Au (M series) confirming the small and big particles are Au S16

Figure S15. (left) TEM image of 0.8Au-PFBPy/SWCNT synthesized by a slow diffusion method. (right) The corresponding CO₂ reduction performance S17

Figure S16. Summary of the composite prepared with sorted tubes containing more metallic tubes. (**a**) TEM image of 1.65Au-PFBPy/sc-SWCNT, where the sc-purity of sorted tubes was ~98% ($f = 0.347$), (**b**) the corresponding size histogram, showing a mean size of 1.15 ± 0.21 nm. The corresponding CO₂ reduction performance, FE CO (**c**), and FE H₂ (**d**), compared to its counterparts where the sorted tubes had a sc-purity $\geq 99.9\%$ ($f \geq 0.40$). S18

Figure S17. Schematic illustration of the electrochemical cell for CO₂ reduction reaction S19

Table S1. Summary of eCO₂RR performance catalyzed by Au nanocrystals and nanoclusters

Electrocatalyst	Mass Loading, Mass Activity, and Selectivity	Stability	Ref./Year
Oxide-Derived Au NPs	m(Au) = 7.5mg/cm ² on Au foil electrode J _{CO} = 0.43A/g, FE CO = 98%, at -0.4V vs RHE	8h at -0.4V vs RHE	1, 2012
Au NCs 8 nm	m(Au) unknown J _{CO} = 3A/g, FE CO = 97%, at -0.52V vs RHE	N/A	2, 2013
Au Nanowires	m(total) = 82mg/cm ² on carbon paper J _{CO} = 1.84A/g, FE CO = 94%, at -0.35V vs RHE	12h at -0.35V vs RHE	3, 2014
Au NCs/MWCNTs (~18.3 nm)	m(Au) = 0.008mg/cm ² twisted to a yarn J _{CO} = 15A/g, FE CO = 94%, at -0.5V vs RHE	12h at -0.5V vs RHE	4, 2015
Au NPs on graphene nanoribbon	m(Au) = 0.3mg/cm ² on carbon paper J _{CO} = 36.8A/g, FE CO = 90%, at -0.7V vs RHE	24h at 8 mA/cm ²	5, 2017
Au NPs on mesoporous carbon	m(total) = 0.097mg/cm ² on carbon paper J _{CO} = 12.8A/g, FE CO = 80%, at -0.55V vs RHE	N/A	6, 2018
AuNPs/Pyridine/MWCNTs	m(Au) = 0.078mg/cm ² on carbon paper J _{CO} = 251A/g, FE CO = 93%, at -0.98V vs RHE	10h at -0.98V vs RHE	7, 2019
AuNPs on MWCNTs (~4.3 nm)	m(Au) = 0.2mg/cm ² J _{CO} = 50.8A/g, FE CO = 97%, at -0.8V vs RHE	30h at -0.8V vs RHE	8, 2023
Au ₂₈ clusters/CNTs	m(total) = 0.5mg/cm ² J _{CO} = ~70A/g, FE CO = 96.5%, at -0.57V vs RHE	40h at -0.69V vs RHE	9, 2021
Au ₂₅ clusters	m(Au) unknown J _{tot} = ~14.3 mA/cm ² , FE CO = 99.6%, at -0.89V vs RHE	unknown	10, 2012
Au ₂₄ clusters	m(Au) = 0.066mg/cm ² on carbon paper J _{CO} = 1360A/g under 100 mA/cm ² , FE CO = 90% at -3.2V overpotential	>100h	11, 2022
Au ₁₃ clusters	m(Au) = 50 mg/cm ² , J _{CO} = 1800A/g, FE CO = 90%, under 100 mA/cm ² m(Au) = 5 mg/cm ² , J _{CO} = 7500A/g, FE CO = ~75%, under 100 mA/cm ²	>100h	12, 2024
1-nm AuNCs/PFBPy/sc-SWCNTs	m(total) = 0.05mg/cm ² , m(Au) = 0.0114mg/cm ² on carbon paper J _{CO} = 5610 A/g, FE CO = 64%, under 100 mA/cm ² , FE CO: 86% at 25 mA/cm ²	25h at 100 mA/cm ²	This work

Note:

$$\text{mass activity} = \frac{\text{Faradaic Efficiency} \times \text{Total current}}{\text{Mass loading}}$$

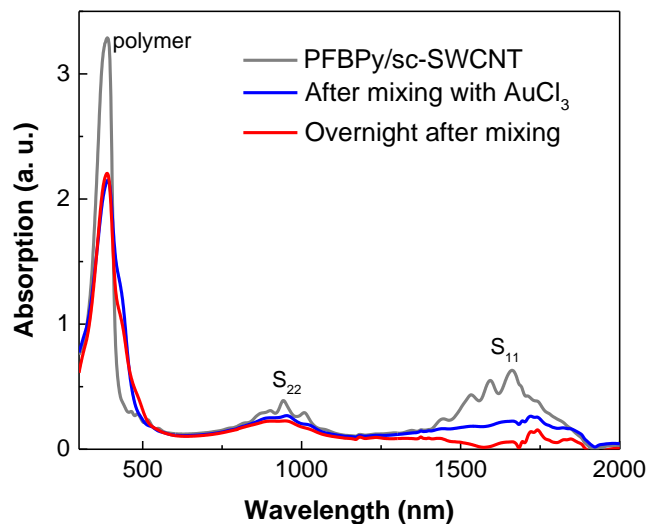


Figure S1. Absorption spectra of PFBPy/sc-SWCNT in THF before mixing, right after mixing, and overnight after mixing with AuCl₃ THF solution, [Au]/[BPy] = 1.65:1 molar ratio.

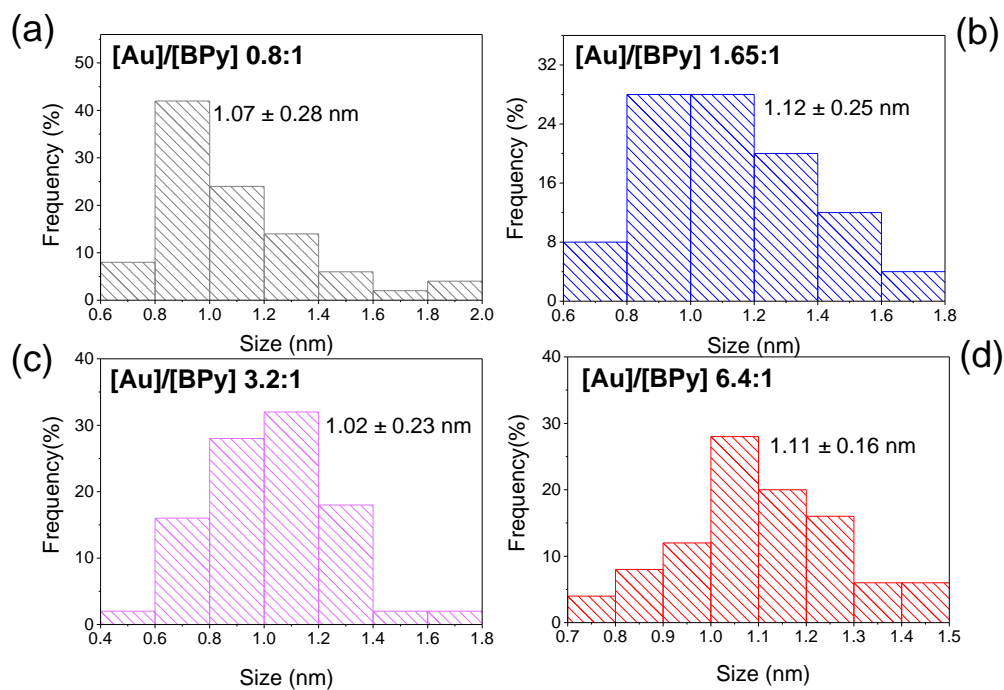


Figure S2. Size distribution histograms of AuNCs synthesized with varied [Au]/[BPy] molar ratios.

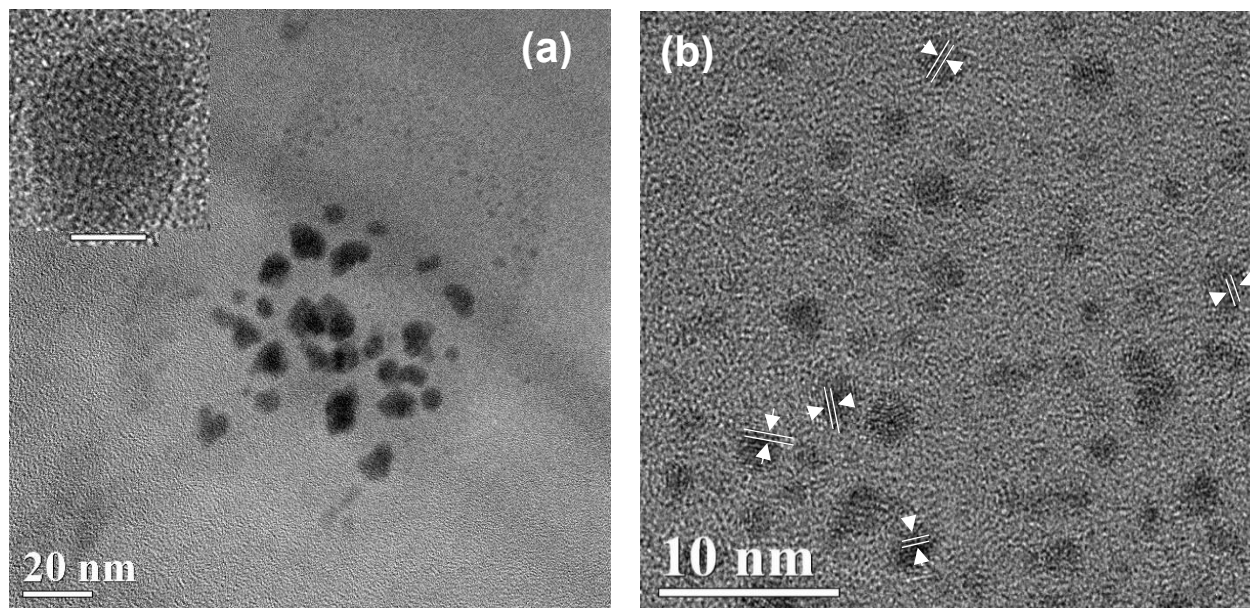


Figure S3. (a) TEM image of 1.65Au-PFDD/SWCNT sample, the inset (scale bar = 5 nm) shows one crystal with lattice fringes. (b) High-resolution TEM image of 6.4Au-PFBPy/SWCNT sample. The measured d-spacing as indicated by arrows is ~ 0.22 nm which corresponds to the Au (111) plane d-spacing.

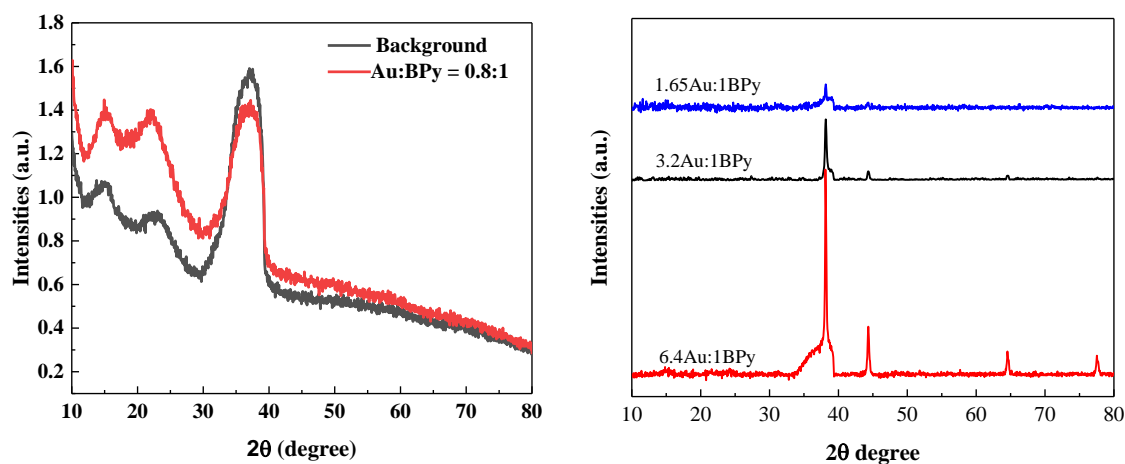


Figure S4. XRD spectra of substrate background and 0.8Au-PFBPy/SWCNTs sample (left), and original spectra for the samples with 1.65Au-, 3.2Au-, and 6.4Au-PFBPy/SWCNTs (right).

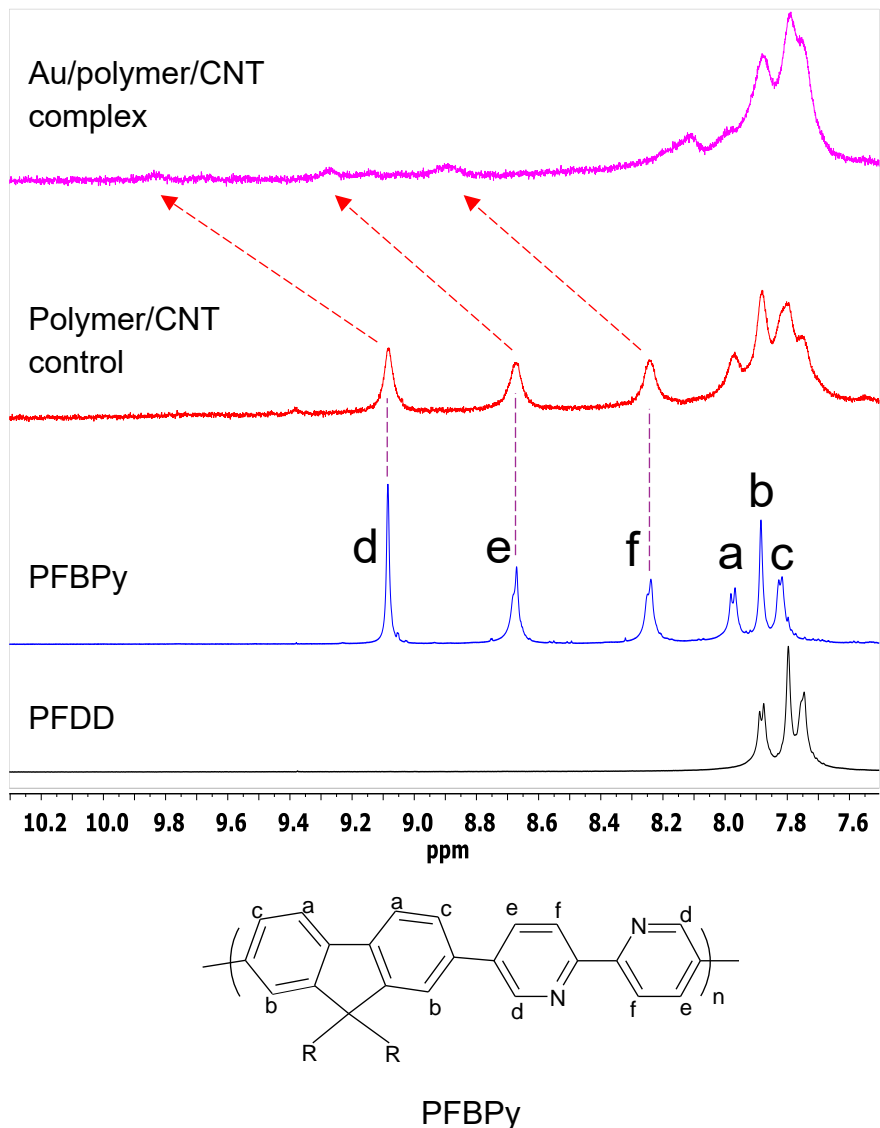


Figure S5. The comparison of $^1\text{H-NMR}$ spectra in the backbone region of PFDD, PFBPy, polymer/CNT control, and AuNCs-polymer/CNT complex (Au:BPY = 3.7:1) in THF- d_8 . The peaks of **a** to **c** are assigned to the fluorene unit, and **d** to **f** to the bipyridine (BPy) unit.

In free polymers, these peaks are sharp with coupling features, while the peaks are relatively broad without coupling features in the control sample, indicating the interaction between the backbone and the CNT surface. After addition of AuCl_3 solution with vigorous shaking, the resulted complex reveals a significant downfield shift, indicating electron de-shielded thanks to the electron donation from BPy unit to AuNCs.

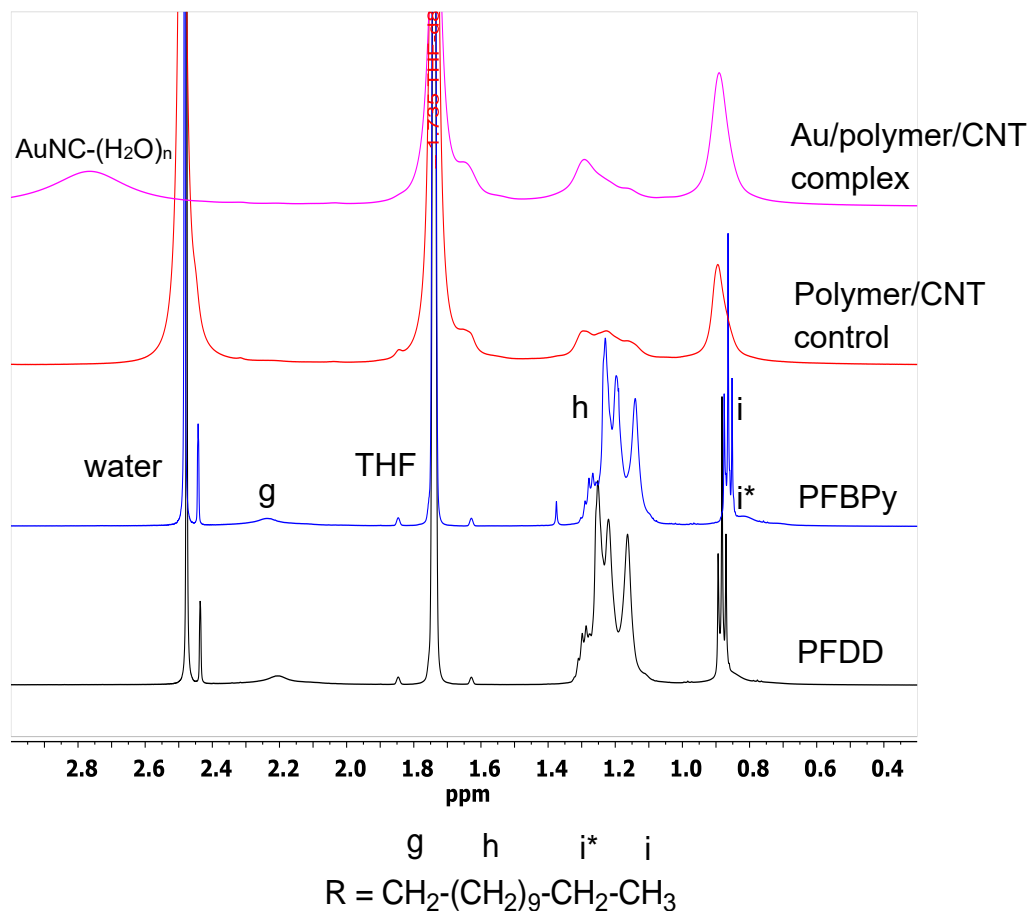


Figure S6. The comparison of $^1\text{H-NMR}$ spectra in the side chain region of PFDD, PFBPy, polymer/CNT control, and AuNCs-polymer/CNT complex (Au:BPpy = 3.7:1) in THF- d_8 . The peaks of **g** to **i** are assigned as shown at the bottom.

In free polymers, **h** and **i** are sharp with coupling features, while they are relatively broad without coupling features in the control sample, indicating the interaction between the side chain and CNT surface. The relative area ratio of **h** over (**i**+**i***) is smaller in the control sample than in the free polymers, indicating the end group experiences less restriction from the tube. **g** is barely detectable in the control sample, indicating severe restriction from the tube. The complex is similar to the control sample except that the water peak diminishes and shifts toward downfield due to water molecules coordination with AuNCs.

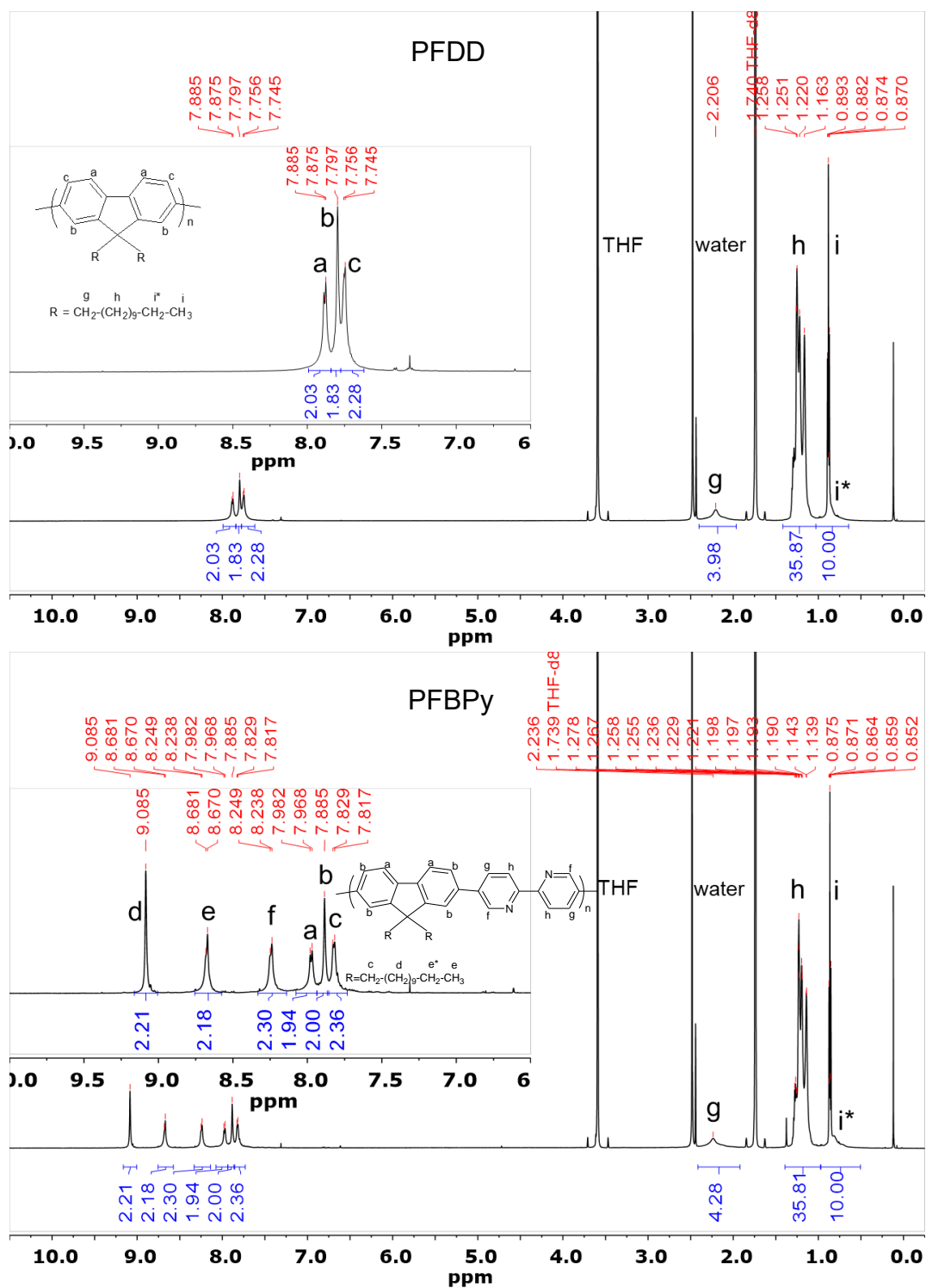


Figure S7. $^1\text{H-NMR}$ spectra of PFDD (top) and PFBPY (bottom) in THF- d_8 . The insets are the magnified backbone regions.

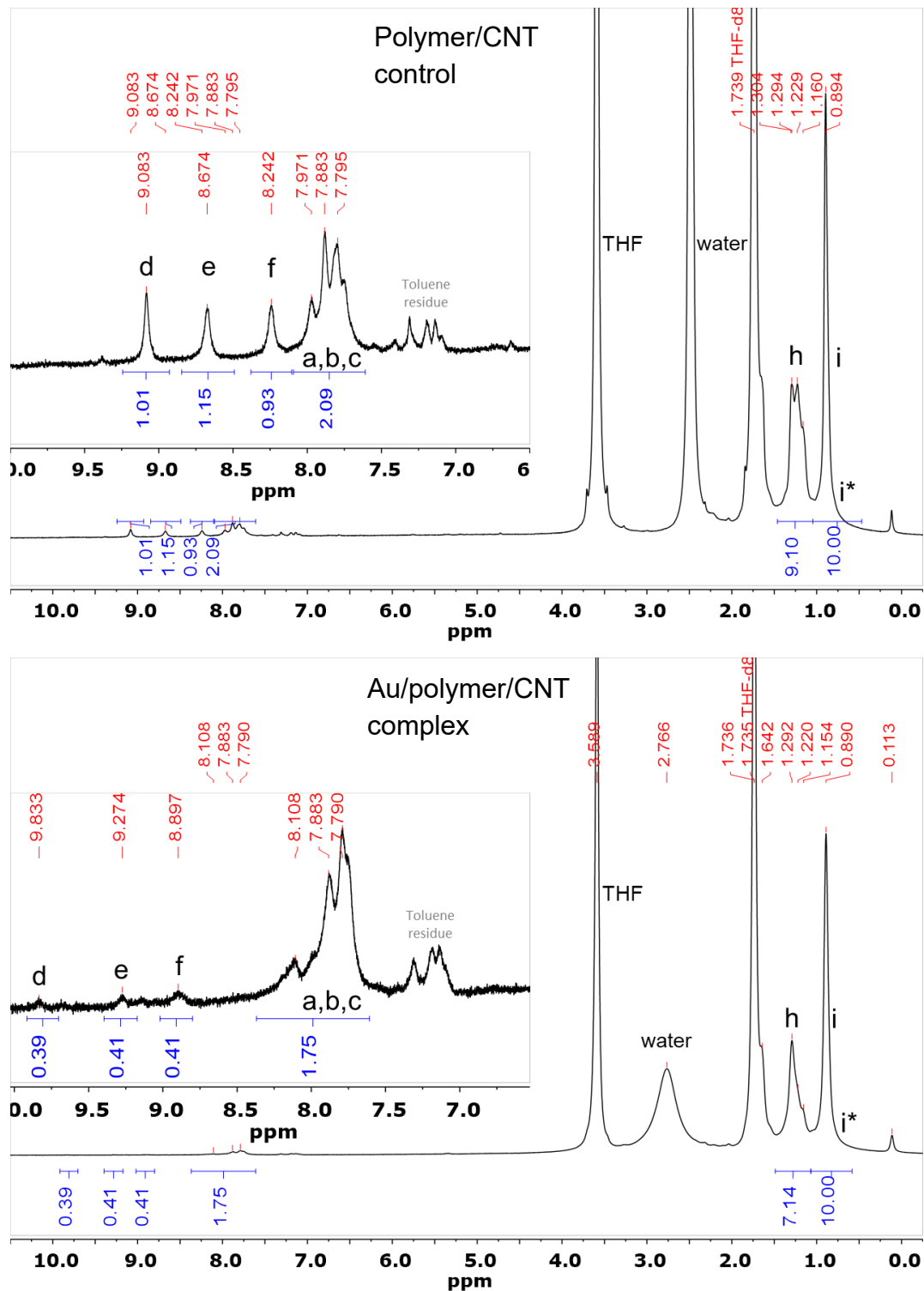


Figure S8. ^1H -NMR spectra of polymer/CNT control (top) and AuNCs-polymer/CNT complex (Au:BPY = 3.7:1) (bottom) in THF- d_8 . The insets are the magnified backbone regions.

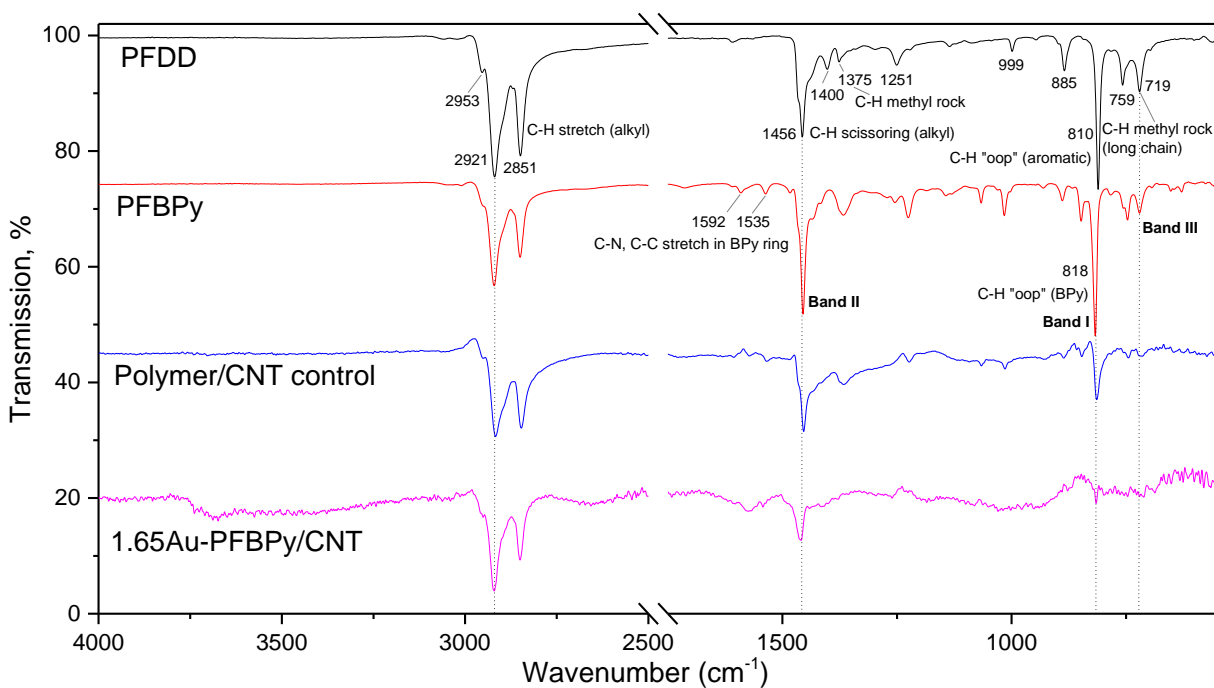


Figure S9. The comparison of FT-IR spectra of PFDD, PFBPy, polymer/CNT control, and 1.65Au-PFBPy/CNT composite.

As compared to the free polymers, the control sample reveals significant intensity reduction in ring C-H “oop” (Band I), C-H scissoring (alkyl sidechain, Band II), and C-H methyl rock (alkyl sidechain, Band III), indicating the interaction of both backbone and sidechain with the CNT surface.

As compared to the control sample, the composite reveals further intensity reduction in these bands, especially in Band I, indicating the coordination between AuNCs and PFBPy severely restrict the motion of BPy units.

The peak assignment of PFBPy is referred to:

Strukl, J. S.; Walter, J. L. Infrared and Raman Spectra of Heterocyclic Compounds-III The Infrared Studies and Normal Vibrations of 2,2'-bipyridine. *Spectrochimica Acta* **1971**, *27A*, 209 - 221.

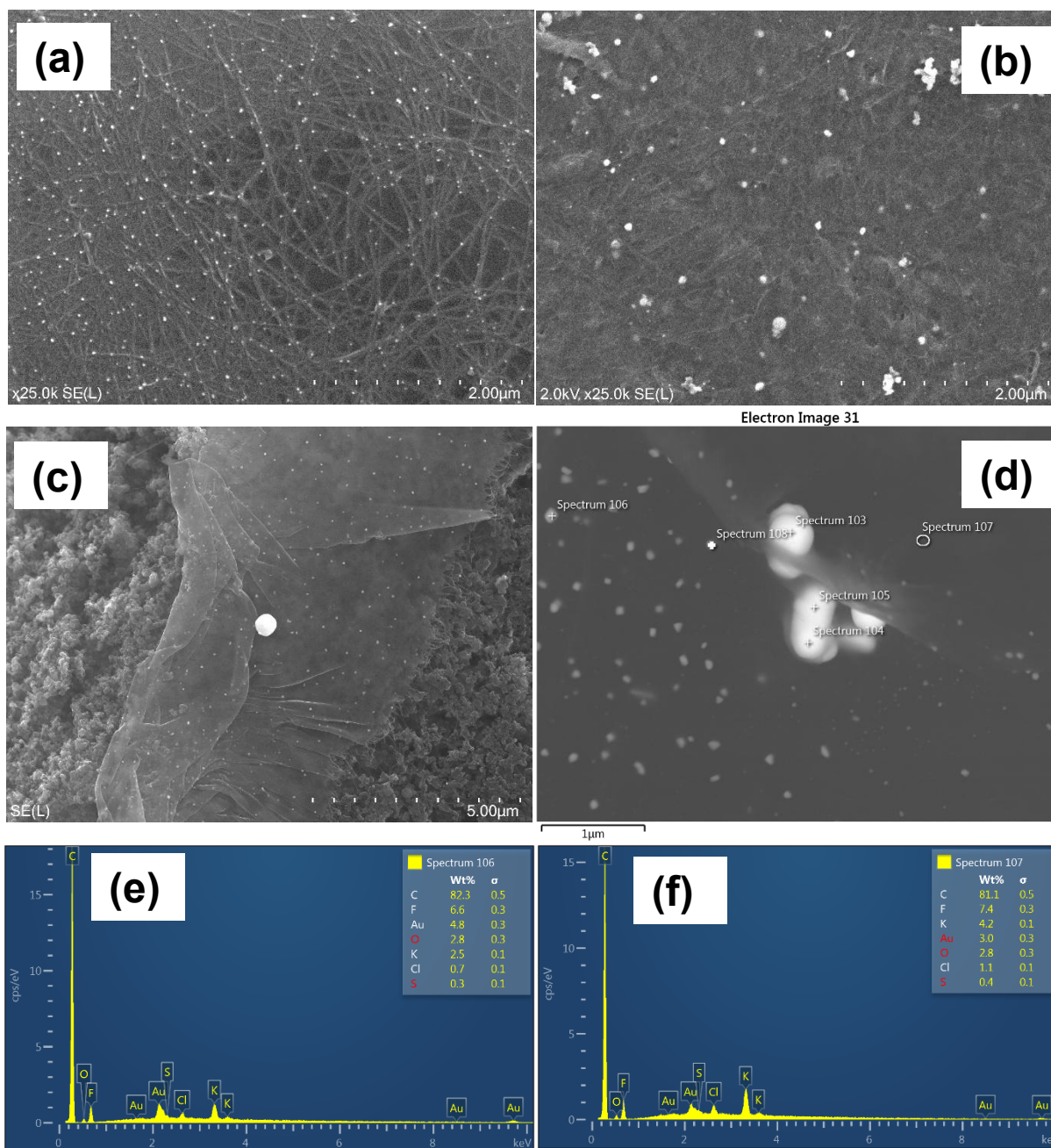


Figure S10. SEM images of Sample 1.65Au-PFBPy/SWCNTs dried at room temperature on silicon wafer (a), thermal treated at 270 °C for 3 hours on silicon wafer (b) and on carbon paper (c and d). Au was detected from spectrum 103 to spectrum 108 labelled in (d). Spectrum 106 and spectrum 107 are presented in (e) and (f), respectively. It is worth noting that Au was detected in spectrum 107, which means small AuNCs exist in the composite matrix although they are invisible under SEM.

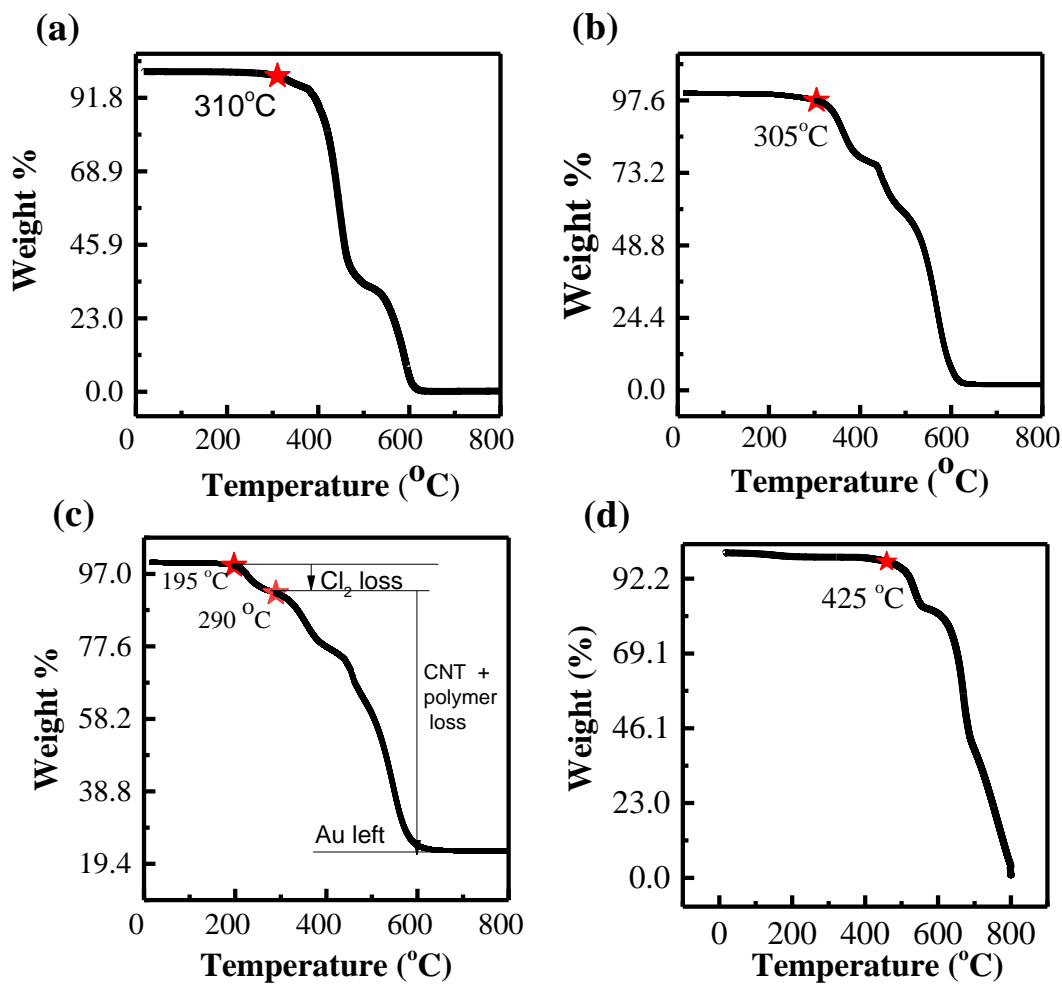


Figure S11. TGA curves of (a) PFDD, (b)PFBPY with SWCNTs, (c) 1.65Au-PFBPY/SWCNTs (22.6% left as Au, theoretically Au wt% is 23.7%). (d) Sigracet 39 BB carbon paper. All samples were heated in air from room temperature to 800 °C ramped in 10 °C/min, and held at 800 °C for 15 min.

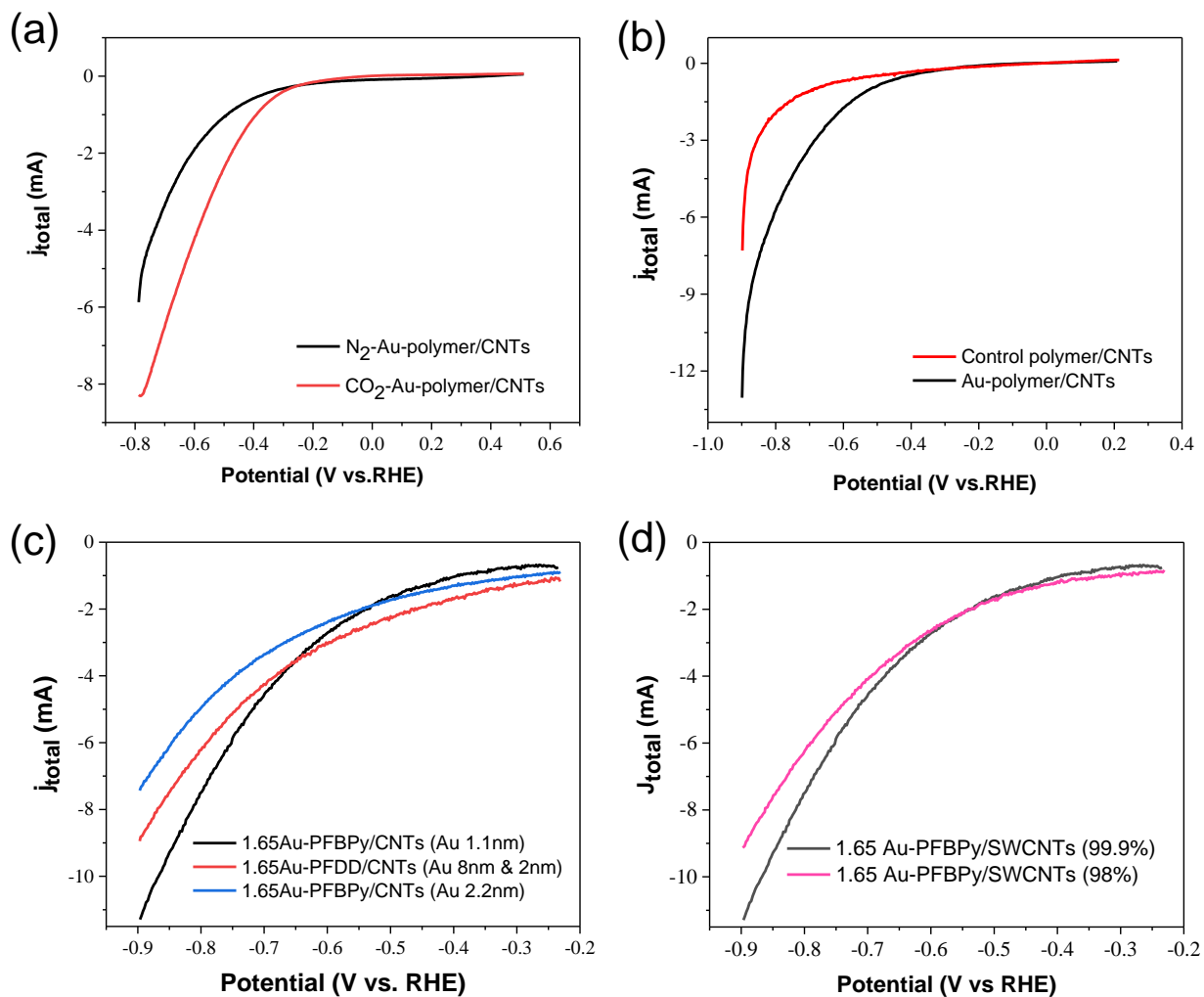


Figure S12. (a) Linear sweep voltammetry (LSV) curves for the 1.65Au-PFBPy/SWCNTs sample in both saturated N₂ and CO₂ environments with a pH of 8.8 and 6.8, respectively. (b) LSV curves for 1.65Au-PFBPy/SWCNTs and polymer/SWCNTs control sample measured in a saturated CO₂ environment. (c) LSV curves for 1.65Au-PFBPy/SWCNTs (Au 1.1 nm), 1.65Au-PFDD/SWCNTs (polydisperse Au, 8 nm & 2 nm) 1.65Au-PFBPy/SWCNTs (AuNCs 2.2 nm, synthesized with a slow diffusion rate) in a saturated CO₂ environment. (d) LSV curves for 1.65Au-PFBPy/SWCNTs prepared with 99.9% vs 98% sc-purity in a saturated CO₂ environment.

Table S2. Impedance measured at 150 kHz for samples with different drying temperature or tube compositions.

Samples	Impedance (R_s)
1.65Au-PFBPy/SWCNTs (sc-purity 99.9%), dried at R.T.	4.4 Ω
1.65Au-PFBPy/SWCNTs (sc-purity 99.9%), dried at 270 °C	0.8 Ω
1.65Au-PFBPy/SWCNTs (sc purity 98%), dried at 270 °C	1.1 Ω

Note: Electrochemical impedance spectra (EIS) were measured in a two-electrode and two-terminal setup, where R_s is the solution resistance or ohmic resistance for the whole system. The same membrane, anode, and electrolyte were used for different cathodes, therefore the difference of the R_s under high frequency was considered coming from the different conductivity/resistance of cathode.

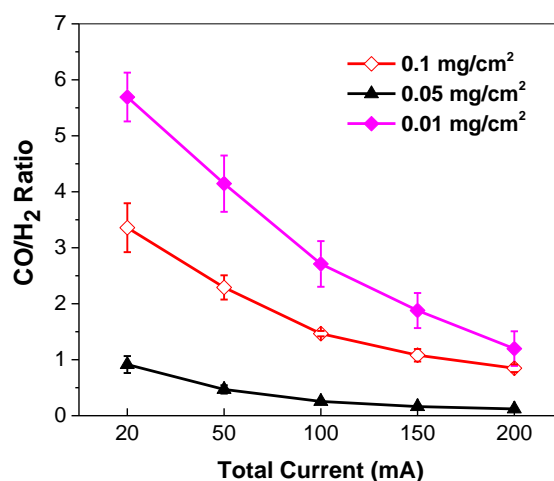


Figure S13. The CO/H₂ ratio changes as a function of total current for various catalyst loading.

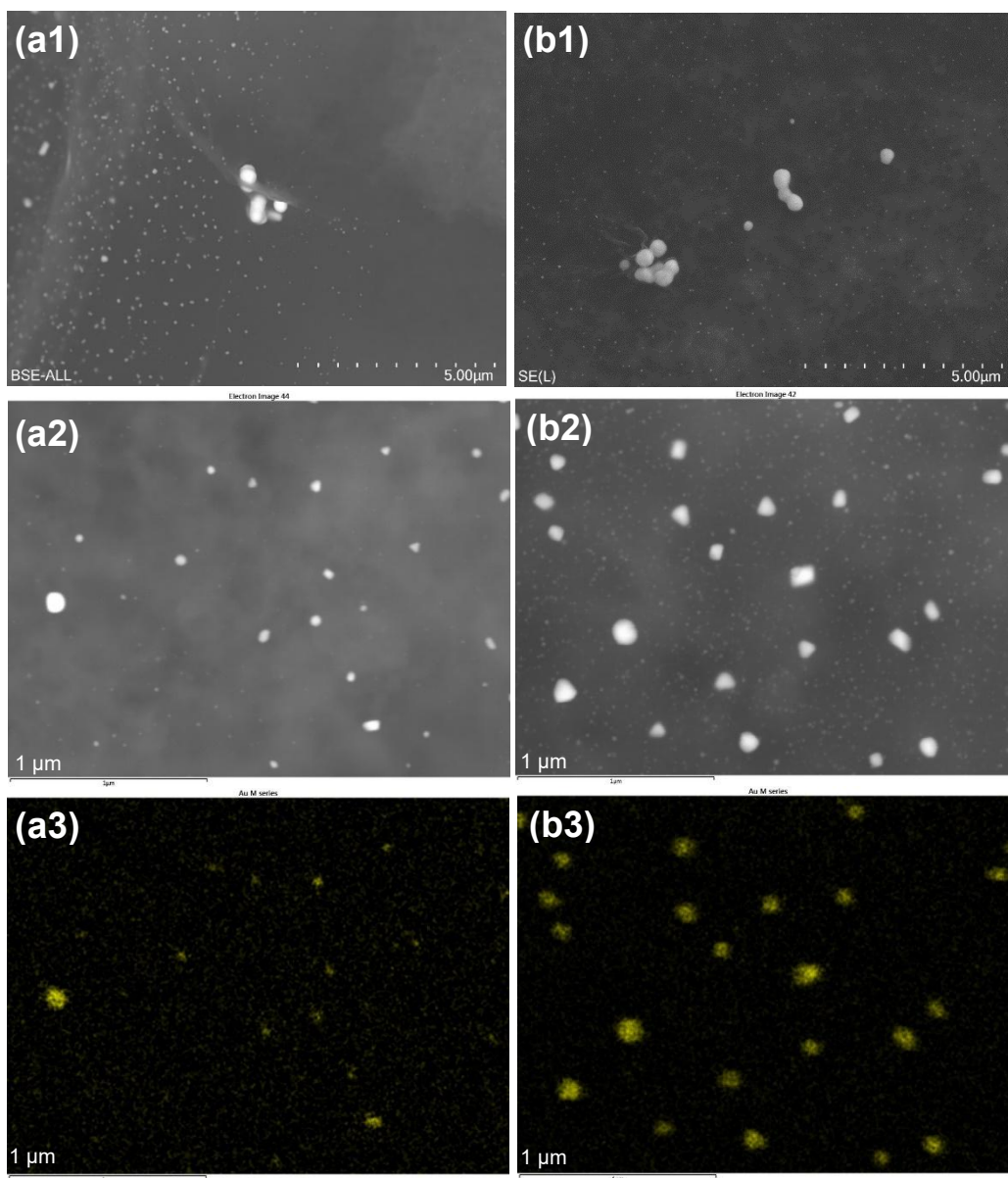


Figure S14. SEM images of Sample 1.65Au-PFBPy/SWCNTs after thermal treated at 270 °C for 3 hours on carbon paper before (a1) and after (b1) electrolysis (~3 hours). One local area showing numerous small particles with scattering big particles before (a2) and after (b2) electrolysis. The corresponding x-ray mapping for Au (M series) confirming the small and big particles are Au before (a3) and after (b3) electrolysis.

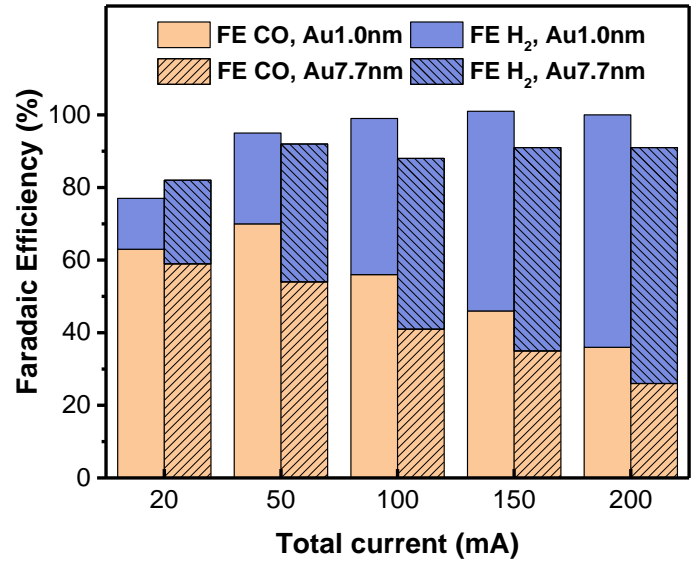
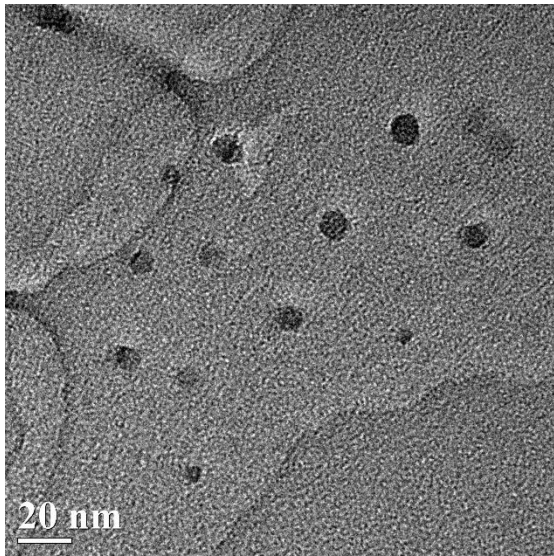


Figure S15. (left) TEM image of 0.8Au-PFBPy/SWCNTs synthesized by a slow diffusion method (size 7.7 ± 2.2 nm). (right) The corresponding CO₂ reduction performance compared to its counterpart synthesized by a fast diffusion method (size 1.07 ± 0.28 nm).

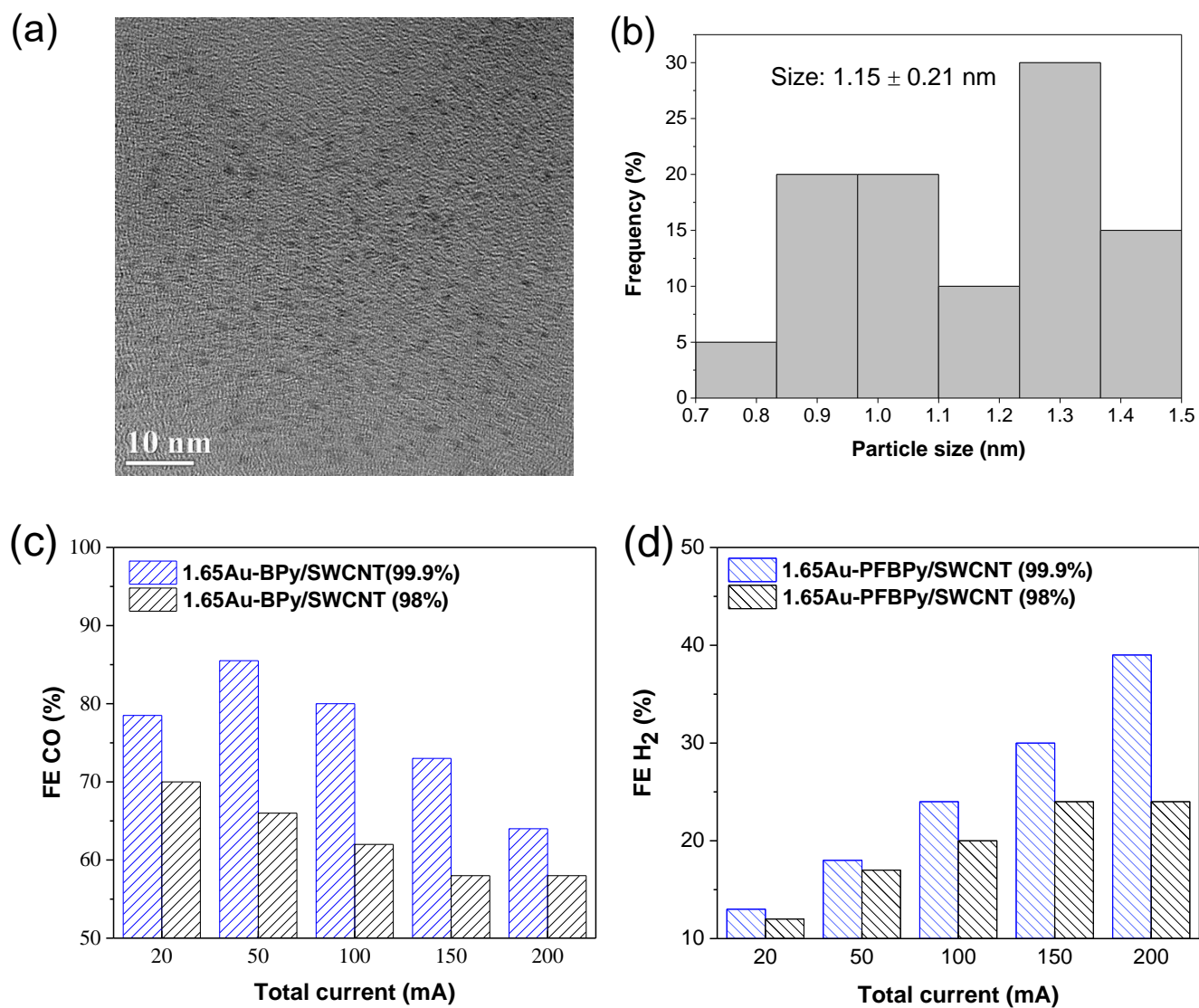


Figure S16. Summary of the composite prepared with sorted tubes containing more metallic tubes. **(a)** TEM image of 1.65Au-PFBPy/sc-SWCNT, where the sc-purity of sorted tubes was $\sim 98\%$ ($\phi = 0.347$), **(b)** the corresponding size histogram, showing a mean size of 1.15 ± 0.21 nm. The corresponding CO₂ reduction performance, FE CO **(c)**, and FE H₂ **(d)**, compared to its counterparts where the sorted tubes had a sc-purity $\geq 99.9\%$ ($\phi \geq 0.40$).

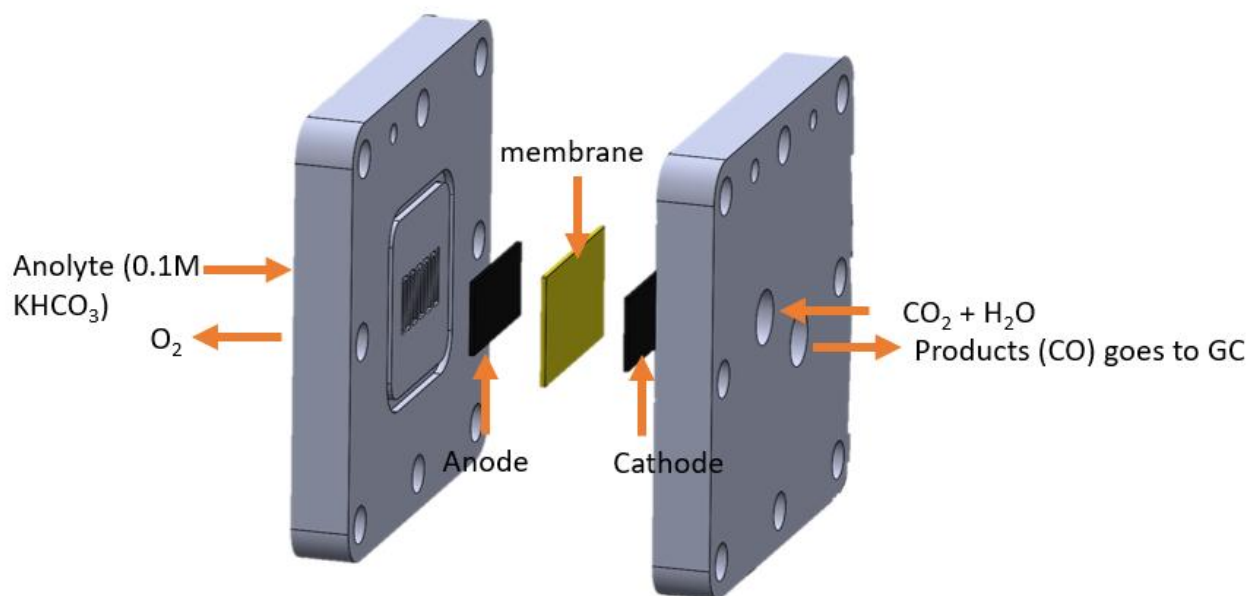


Figure S17. Schematic illustration of the electrochemical cell for CO₂ reduction reaction.

References in Table S1:

1. Chen, Y.; Li, C. W.; Kanan, M. W. Aqueous CO₂ Reduction at Very Low Overpotential on Oxide-Derived Au Nanoparticles. *J. Am. Chem. Soc.* **2012**, *134* (49), 19969–19972. <https://doi.org/10.1021/ja309317u>.
2. Zhu, W.; Michalsky, R.; Metin, Ö.; Lv, H.; Guo, S.; Wright, C. J.; Sun, X.; Peterson, A. A.; Sun, S. Monodisperse Au Nanoparticles for Selective Electrocatalytic Reduction of CO₂ to CO. *J. Am. Chem. Soc.* **2013**, *135* (45), 16833–16836. <https://doi.org/10.1021/ja409445p>.
3. Zhu, W.; Zhang, Y.-J.; Zhang, H.; Lv, H.; Li, Q.; Michalsky, R.; Peterson, A. A.; Sun, S. Active and Selective Conversion of CO₂ to CO on Ultrathin Au Nanowires. *J. Am. Chem. Soc.* **2014**, *136* (46), 16132–16135. <https://doi.org/10.1021/ja5095099>.
4. Feng, X.; Jiang, K.; Fan, S.; Kanan, M. W. Grain-Boundary-Dependent CO₂ Electroreduction Activity. *J. Am. Chem. Soc.* **2015**, *137* (14), 4606–4609. <https://doi.org/10.1021/ja5130513>.
5. Rogers, C.; Perkins, W. S.; Veber, G.; Williams, T. E.; Cloke, R. R.; Fischer, F. R. Synergistic Enhancement of Electrocatalytic CO₂ Reduction with Gold Nanoparticles Embedded in Functional

- Graphene Nanoribbon Composite Electrodes. *J. Am. Chem. Soc.* **2017**, *139* (11), 4052–4061. <https://doi.org/10.1021/jacs.6b12217>.
6. Miola, M.; Hu, X.-M.; Brandiele, R.; Bjerglund, E. T.; Grønseth, D. K.; Durante, C.; Pedersen, S. U.; Lock, N.; Skrydstrup, T.; Daasbjerg, K. Ligand-Free Gold Nanoparticles Supported on Mesoporous Carbon as Electrocatalysts for CO₂ Reduction. *J. CO₂ Utilization* **2018**, *28*, 50–58. <https://doi.org/10.1016/j.jcou.2018.09.009>.
 7. Ma, Z.; Lian, C.; Niu, D.; Shi, L.; Hu, S.; Zhang, X.; Liu, H. Enhancing CO₂ Electroreduction with Au/Pyridine/Carbon Nanotubes Hybrid Structures. *ChemSusChem* **2019**, *12* (8), 1724–1731. <https://doi.org/10.1002/cssc.201802940>.
 8. Wang, A.; Zhu, Y.; Sun, J.; Hu, S.; Zhang, X.; Niu, D. The Nature of Interaction between Au and Heteroatoms-Doped Carbon Nanotubes: Size and Electronic Effects on CO₂ Electroreduction. *Appl. Surf. Sci.* **2023**, *635*, 157692. <https://doi.org/10.1016/j.apsusc.2023.157692>.
 9. Yuan, S.; He, R.; Han, X.; Wang, J.; Guan, Z.; Wang, Q. Robust Gold Nanocluster Protected with Amidinates for Electrocatalytic CO₂ Reduction. *Angew. Chem. Int. Ed.* **2021**, *60* (26), 14345–14349. <https://doi.org/10.1002/anie.202103060>.
 10. Kauffman, D. R.; Alfonso, D.; Matranga, C.; Qian, H.; Jin, R. Experimental and Computational Investigation of Au₂₅ Clusters and CO₂: A Unique Interaction and Enhanced Electrocatalytic Activity. *J. Am. Chem. Soc.* **2012**, *134* (24), 10237–10243. <https://doi.org/10.1021/ja303259q>.
 11. Kulkarni, V. K.; Khiarak, B. N.; Takano, S.; Malola, S.; Albright, E. L.; Levchenko, T. I.; Aloisio, M. D.; Dinh, C.-T.; Tsukuda, T.; Häkkinen, H.; Crudden, C. M. N-Heterocyclic Carbene-Stabilized Hydrido Au₂₄ Nanoclusters: Synthesis, Structure, and Electrocatalytic Reduction of CO₂. *J. Am. Chem. Soc.* **2022**, *144* (20), 9000–9006. <https://doi.org/10.1021/jacs.2c00789>.
 12. Levchenko, T. I.; Yi, H.; Aloisio, M. D.; Dang, N. K.; Gao, G.; Sharma, S.; Dinh, C.-T.; Crudden, C. M. Electrocatalytic CO₂ Reduction with Atomically Precise Au₁₃ Nanoclusters: Effect of Ligand Shell on Catalytic Performance. *ACS Catalysis* **2024**, *14* (6), 4155–4163. <https://doi.org/10.1021/acscatal.3c06114>.